INTERNATIONAL JOURNAL FOR NUMERICAL METHODS IN FLUIDS
Int. J. Numer. Meth. Fluids 2003; **41**:225–250 (DOI: 10.1002/fld.429)

Solution of the hyperbolic mild-slope equation using the finite volume method

J. Bokaris*,† and K. Anastasiou‡

Department of Civil Engineering, Imperial College of Science, Technology and Medicine, Imperial College Road, London SW7 2BU, U.K.

SUMMARY

A finite volume solver for the 2D depth-integrated harmonic hyperbolic formulation of the mild-slope equation for wave propagation is presented and discussed. The solver is implemented on unstructured triangular meshes and the solution methodology is based upon a Godunov-type second-order finite volume scheme, whereby the numerical fluxes are computed using Roe's flux function. The eigensystem of the mild-slope equations is derived and used for the construction of Roe's matrix. A formulation that updates the unknown variables in time implicitly is presented, which produces a more accurate and reliable scheme than hitherto available. Boundary conditions for different types of boundaries are also derived. The agreement of the computed results with analytical results for a range of wave propagation/transformation problems is very good, and the model is found to be virtually paraxiality-free. Copyright © 2003 John Wiley & Sons, Ltd.

KEY WORDS: coastal wave modelling; mild-slope equation; finite volume method; unstructured triangular mesh; Roe's flux function; implicit time integration

1. INTRODUCTION

Accurate numerical modelling of water wave propagation from offshore to coastal regions is of paramount importance to coastal, port and environmental engineers. Such models can greatly simplify and expedite the design of coastal structures and the evaluation of their influence on the surrounding environment.

As waves travel towards the coastline they are transformed by the combined effect of complex physical processes. Initial efforts in nearshore wave modelling tended to calculate separately the effect of each one of these processes resulting sometimes in erroneous predictions (e.g. unrealistically high wave heights predicted by wave ray models in caustic zones).

* Correspondence to: J. Bokaris, 6 Paraschou Road, P. Psychiko, 154 52, Athens, Greece.
† Research Student.
‡ Reader in Coastal Engineering.

Contract/grant sponsor: Commission of the European Communities; contract/grant number MAS3-CT97-5052

Received January 2000
Revised 21 April 2002

This was mainly due to the fact that the equations used to model the problem were over-simplified and did not describe the physics adequately. The need to include simultaneously more of the physical processes in order to describe more realistically the transformation of water waves was evident.

Berkhoff [1] attempted to calculate the combined effect of the processes of diffraction, refraction, shoaling and reflection. In the depth-integrated elliptic mild-slope equation he derived, small-amplitude wave theory was used under the assumption of a gently sloping seabed. In Berkhoff's equation the wave energy is correctly transported by the group celerity rather than the phase celerity and can therefore properly express wave shoaling and refraction [2]. Booij [3] numerically investigated the 'mild-slope' assumption for a plane slope and concluded that the equation could be used for a slope up to 1:3 for waves propagating normal to the depth contours, and up to 1:1 for propagation parallel to the depth contours.

Berkhoff's computationally expensive elliptic mild-slope equation, led Radder [4] and other researchers to derive more efficient parabolic approximations that omitted the reflected field and required paraxiality (wave propagating in the direction of one of the computational axes). Kirby [5] used a minimax approximation in the parabolic formulation in order to allow for large angles of wave propagation. In tackling paraxiality Isobe [6] introduced a curvilinear co-ordinate system, corresponding to wave rays and fronts appropriate to a simplified bottom topography, that resulted in no caustics being formed. It is noted that such an over-simplification of the bathymetry might omit essential bathymetric features. Li and Anastasiou [7] noted that reflections could be taken into account in the parabolic equation method, but in that case additional computational resources were required. The effort to overcome the limitations of paraxiality, as well as the omission of the reflected wave field render the parabolic equation method no longer computationally viable. Both limitations are severe and cannot be overlooked since areas of considerable reflection arise in the vicinity of surface piercing obstacles (e.g. harbours, breakwaters, etc.), which are very frequently encountered in coastal engineering applications. Furthermore, the investigation of the behaviour of a structure under different angles of wave incidence may be required. Having to re-orient the computational axes each time in the direction of wave propagation is troublesome. Finally, a paraxiality bound model does not constitute an appropriate basis for modelling directional irregular sea states.

Using a finite difference method Copeland [8] solved the harmonic hyperbolic form of the mild-slope equation which does not neglect the reflected field and requires reduced computing effort compared with the elliptic form. For an horizontal bottom, the hyperbolic system of equations reduces to the linearized equations of continuity and motion derived by Ito and Tanimoto [9] in order to predict the time-evolution of long waves.

In view of the above observations, the hyperbolic form of the mild-slope equation was selected as the modelling basis in the present study. In addition the efficient discretization of irregular domains often associated with realistic situations, was considered an essential part of the present study. The finite difference method does not offer great flexibility with respect to discretizing irregular domains. The finite element method can deal with irregular boundaries but is more suitable for the elliptic formulation of the mild-slope equation. Anastasiou and Chan [10] recently solved the full system of the depth-integrated 2D shallow water equations and the 2D incompressible Navier–Stokes equations [11] using a finite volume technique on unstructured triangular meshes whereby the boundaries are dealt with the method of characteristics. The method is applicable to domains of arbitrary complexity and can deal with

discontinuities, inflows and outflows, as well as wall boundaries. The accuracy of the results Anastasiou and Chan [10, 11] reported is impressive. Consequently, a similar methodology for the solution of the mild-slope equation for linear, regular waves, has been adopted herein. It was decided to adopt a linear governing equation in order to keep the computational cost relatively low and in view of the fact that the linear mild-slope equation predicts with a satisfactory accuracy the wave height and wave direction. If it is desired to compute the water particle kinematics to a high degree of accuracy, then the waveheights derived from the linear solution of the mild-slope equation may be used in conjunction a high-order non-linear wave theory.

The present numerical model is second-order accurate and is based on a cell-centred finite volume upwind scheme implemented on an unstructured triangular mesh. The irregular domain is initially discretized using the versatile automatic unstructured triangular mesh generator of Anastasiou and Chan [12]. Roe's [13, 14] flux function is subsequently used to evaluate the inviscid fluxes at the triangular cell edges, assuming a local Riemann problem in the direction normal to the cell edge. The eigensystem required for the evaluation of Roe's matrix is derived from the flux Jacobian matrix in the direction normal to the cell edge. To the best of the authors' knowledge such a solution of the mild-slope equation is reported herein for the first time.

2. FINITE VOLUME DISCRETIZATION OF THE 2D MILD-SLOPE EQUATIONS

Assuming an incompressible and homogeneous fluid, irrotational flow, no viscosity, slowly varying bathymetry and small-amplitude waves, the harmonic form of the mild-slope equation is given by the second-order partial differential equation

$$\nabla \cdot (cc_{\mathrm{g}} \nabla \eta) - \frac{c_{\mathrm{g}}}{c} \frac{\partial^2 \eta}{\partial t^2} = 0 \tag{1}$$

where c, c_{g} are the wave celerity and the group celerity, respectively, as defined by small-amplitude wave theory, η is the free surface elevation of the water, $\nabla = (\partial/\partial x)\mathbf{i} + (\partial/\partial y)\mathbf{j}$, i.e. the horizontal gradient operator. Equation (1) can be decomposed into the following system of first-order linear partial differential equations, identical to Copeland's [8] hyperbolic formulation

$$\begin{aligned} \nabla \cdot \mathbf{Q} + \frac{c_{\mathrm{g}}}{c} \frac{\partial \eta}{\partial t} &= 0 \\ \frac{\partial \mathbf{Q}}{\partial t} + cc_{\mathrm{g}} \nabla \eta &= 0 \end{aligned} \tag{2}$$

where

$$\begin{aligned} \mathbf{Q} = (q_x, q_y), \quad q_x = \int_{-d}^{0} Zu \, \mathrm{d}z = \frac{cc_{\mathrm{g}}}{g} u_0, \\ q_y = \int_{-d}^{0} Zv \, \mathrm{d}z = \frac{cc_{\mathrm{g}}}{g} v_0, \quad Z = \frac{\cosh k(z+d)}{\cosh kd} \end{aligned} \tag{3}$$

and u, v are the horizontal velocity components in the x, y directions, respectively, and u_0, v_0 are their values at the stillwater level ($z=0$), g is the acceleration due to gravity. In essence $\mathbf{Q}$ is an artificial variable and in order to perform the calculation for the surface elevation, η, using Equations (2) it is not necessary to know the general physical form of $\mathbf{Q}$ (other than its harmonic nature) except where boundary values are required [8]. Equations (2) can be further written in a conservative form suitable for finite volume discretization, generally expressed by

$$\frac{\partial U}{\partial t} + \nabla \cdot \mathbf{F} = G \tag{4}$$

Integration and use of the divergence theorem of Gauss yields

$$\frac{\partial}{\partial t} \int \int_{\Omega} U \, \mathrm{d}\Omega + \oint_{S} \mathbf{F} \cdot \mathbf{n} \, \mathrm{d}S = \int \int_{\Omega} G \, \mathrm{d}\Omega \tag{5}$$

where Ω is the domain of interest, S is the boundary surrounding Ω, $\mathbf{n}$ is the normal vector to S in the outward direction, U is the vector of conserved variables, $\mathbf{F}$ is the vector of flux functions through S, and G is the vector of source terms. As opposed to the shallow water equations [10], the mild-slope system of equations has inviscid fluxes and no viscous fluxes. U, $\mathbf{F}$ and G are given as

$$\mathbf{F} \cdot \mathbf{n} = F = e \cdot n_x + f \cdot n_y$$

$$U = \begin{bmatrix} \eta \\ q_x \\ q_y \end{bmatrix}, \quad e = \begin{bmatrix} cq_x/c_{\mathrm{g}} \\ cc_{\mathrm{g}}\eta \\ 0 \end{bmatrix}, \quad f = \begin{bmatrix} cq_y/c_{\mathrm{g}} \\ 0 \\ cc_{\mathrm{g}}\eta \end{bmatrix}, \quad G = \begin{bmatrix} q_x \partial(c/c_{\mathrm{g}})/\partial x + q_y \partial(c/c_{\mathrm{g}})/\partial y \\ \eta \partial(cc_{\mathrm{g}})/\partial x \\ \eta \partial(cc_{\mathrm{g}})/\partial y \end{bmatrix} \tag{6}$$

where n_x and n_y denote the components of the outward normal vector $\mathbf{n}$ in the x and y directions, respectively. The average value of the conserved variables is stored at the centre of each cell and the edges of each cell define the faces of a triangular control volume. For each triangular control volume, Equation (5) is written as

$$\frac{\partial U_i V_i}{\partial t} = -\oint_{\partial C_i} \mathbf{F} \cdot \mathbf{n} \, \mathrm{d}S + G_i V_i = -R(U_i) \tag{7}$$

where U_i and G_i are the average quantities of cell i stored at the cell centre, ∂C_i and V_i denote the boundary and area of cell i, respectively, and $-R(U_i)$ contains all the right-hand side terms. The integral in Equation (7) may be evaluated as indicated by Equation (4) of Anastasiou and Chan [10].

3. EVALUATION OF INVISCID FLUXES

3.1. Evaluation of inviscid fluxes

For the solution of the hyperbolic system of mild-slope equations with a Godunov-type method, we assume a one-dimensional Riemann (shock tube) problem in the direction normal

to the cell edge. The inviscid numerical intercell fluxes required in Equation (7) are evaluated using Roe's flux function [13, 14] adopted locally at each cell edge, as indicated by Equation (5) of Anastasiou and Chan [10]. The flux Jacobian, J, of the system is given by

$$J = \frac{\partial(\mathbf{F}\cdot\mathbf{n})}{\partial U} = \begin{bmatrix} 0 & cn_x/c_g & cn_y/c_g \\ cc_g n_x & 0 & 0 \\ cc_g n_y & 0 & 0 \end{bmatrix} \tag{8}$$

The eigenvalues of J are

$$\begin{aligned} &\lambda_1 = 0, \quad \lambda_2 = \sqrt{c^2(n_x^2+n_y^2)} = cn, \quad \lambda_3 = -\sqrt{c^2(n_x^2+n_y^2)} = -cn \\ &|\Lambda| = \mathrm{diag}[|\lambda_1|, |\lambda_2|, |\lambda_3|] \end{aligned} \tag{9}$$

The right, R, and left, L, eigenvector matrices are given by

$$R = \begin{bmatrix} 0 & n/c_g & n/c_g \\ n_y & n_x & -n_x \\ -n_x & n_y & -n_y \end{bmatrix}, \quad L = R^{-1} = \begin{bmatrix} 0 & n_y/n^2 & -n_x/n^2 \\ c_g/2n & n_x/2n^2 & n_y/2n^2 \\ c_g/2n & -n_x/2n^2 & -n_y/2n^2 \end{bmatrix} \tag{10}$$

and hence Roe's matrix is given by

$$|A| = \begin{bmatrix} cn & 0 & 0 \\ 0 & cn_x^2/n & cn_x n_y/n \\ 0 & cn_x n_y/n & cn_y^2/n \end{bmatrix} \tag{11}$$

where n is the magnitude of the outward normal vector, $\mathbf{n}$. When $\mathbf{n}$ is a unit vector then $n = 1$. The fact that the eigenvalues of the Jacobian are all real and the right eigenvectors are linearly independent (since the eigenvalues are distinct), confirms that the system of mild-slope equations is strictly hyperbolic.

3.2. Extension of the scheme to obtain second-order accuracy in space

An essential part of the solution process is the determination of the left (interior, $-$) and right (exterior, $+$) Riemann states at each interface. In a first-order space accurate scheme the conserved variables U_i are assumed constant throughout each cell i, i.e. $\nabla U_i = 0$. This means that for all edges, j, of cell i, $U_{i,j}^- = U_i$.

Van Leer [15] introduced the idea of modifying the piecewise constant data in the first-order Godunov method, as a first step to achieving higher accuracy. In order to achieve second-order accuracy in space, a piecewise linear variation of the conserved variables vector is assumed within each cell, i.e. $\nabla U_i = \text{constant}$. For a given cell with centre P_0, for example, the interior Riemann states at the cell vertices, are computed according to expression (10) of Anastasiou and Chan [10], while the gradient of the variables within each cell, ∇U_0, is computed according to Equation (11) of Anastasiou and Chan [10]. The estimated gradient accuracy can be further improved by carrying out a weighted averaging process [16], as indicated by Equations (12) and (13) of Anastasiou and Chan [10].

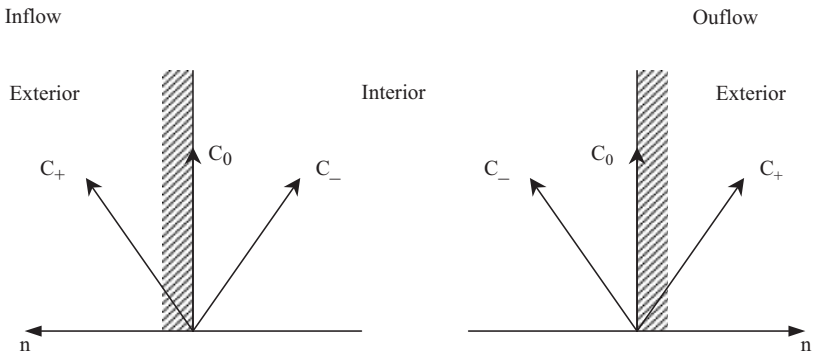

Figure 1. Characteristic directions for the mild-slope equation at inflow and outflow boundaries.

In order to extend the second-order accurate formulation to the boundary cells as well, a row of external elements (phantom cells) which are mirror images of the boundary cells is necessary. Since each phantom cell can have a maximum of two adjacent cells, a closed integration path similar to that of internal cells does not exist, and hence at the phantom cells the scheme is only first-order accurate in space.

4. INITIAL AND BOUNDARY CONDITIONS

Stillwater level conditions are assumed throughout the domain initially, i.e. $\eta = q_x = q_y = 0$.

The eigenvalues and hence the characteristic directions are independent of the conserved variables for the linear mild-slope system, i.e. they are constant with time for each interface and are given by $C_0 = 0$, $C_+ = c$ and $C_- = -c$. For boundary cells this means that there is always one 'wave of information' travelling from outside of the domain to the interior and one travelling from the interior through to the exterior. The third wave ($\lambda_1 = 0$) travels along the boundary and therefore gives no useful information. In Figure 1 the characteristic directions are shown for an inflow and an outflow in the direction normal to a boundary cell edge.

Since each characteristic direction can be considered as transporting a given information (characteristic variable, $W_C = LU$ where L, U as defined in Equations (10) and (6), respectively), the quantities transported from the inside of the domain towards the boundary will influence and modify what goes on at this boundary. Hence, only variables transported from the boundaries towards the interior of the domain may be freely imposed as physical boundary conditions [17]. In both cases of inflow and outflow the C_- characteristic direction is responsible for transporting information to the interior of the computational domain. As a result one physical quantity must be imposed/prescribed. The remaining variables will depend on the computed flow quantities and are, therefore, part of the solution. These variables must satisfy the so-called numerical boundary conditions.

4.1. Driving (offshore) boundary conditions

As already mentioned, the eigenvalues are independent of the conserved variables and hence give no useful information that may be used as boundary conditions. It was therefore necessary

to resort to an extrapolation method for the treatment of boundaries. A zero-order space extrapolation of the characteristic variables was selected [17]. For the boundary edge local co-ordinate system this yields

$$W_C^+ = W_C^- \Rightarrow \begin{bmatrix} -v^+ \\ c_g\eta^+/2 + u^+/2 \\ c_g\eta^+/2 - u^+/2 \end{bmatrix} = \begin{bmatrix} -v^- \\ c_g\eta^-/2 + u^-/2 \\ c_g\eta^-/2 - u^-/2 \end{bmatrix} \tag{12}$$

where u and v are the q_x and q_y components with respect to the local co-ordinate system, '+' denotes an exterior state and '−' an interior state. Prescribing $\eta^+ = \eta_{pr}$ and using the characteristic relations corresponding to the C_0 and C_+ directions (i.e. first and second rows of Equation (12)) to provide the remaining two numerical boundary conditions, we obtain the following set of boundary conditions:

$$\begin{bmatrix} \eta^+ \\ u^+ \\ v^+ \end{bmatrix} = \begin{bmatrix} \eta_{pr} \\ u^- + c_g(\eta^- - \eta_{pr}) \\ v^- \end{bmatrix} \tag{13}$$

The quantities u and v may then be transformed back to the global co-ordinate system. Conditions (13) satisfy the well-posedness criterion [17] indicating that the problem will be well-posed at all boundaries when η is prescribed. Furthermore, knowledge of the physical form of $\mathbf{Q}$ is not required for this set of boundary conditions, since neither q_x nor q_y (i.e. u, v) need to be prescribed in (13).

The sinusoidal surface elevation at each driving boundary node is calculated according to small-amplitude theory using the local wave amplitude and the time delay (cumulative phase) until the disturbance reaches the particular node.

4.2. Outflow (transparent) boundary conditions

At outflows the surface elevation is generally not known and hence cannot be prescribed using Equation (13). To overcome this problem, attempts were made to estimate η_{pr} by extrapolating at each boundary node the known η^- value from the previous time level to the current time level. Unfortunately, these attempts were unsuccessful as the wave form was not predicted accurately, thus introducing spurious oscillations at the boundaries that eventually spread throughout the domain.

The most obvious set of transparent boundary conditions, $U^+ = U^-$, was subsequently tested but, similarly, with no success since the waves were absorbed in the interior of the domain as well, rather than only in the outgoing direction only, as desired.

It may be shown that $Q = c_g\eta = |\mathbf{Q}|$ is a solution of Equation (2) provided that $\nabla c_g = 0$, giving thus a practical relationship for Q in deep water or where the depth is uniform [8]. This relationship, also suggested by Equations (3) (as $c_g\eta = cc_g u_{0-r}/g$, where u_{0-r} is the stillwater level particle velocity in the direction of wave propagation r), finally provided adequate

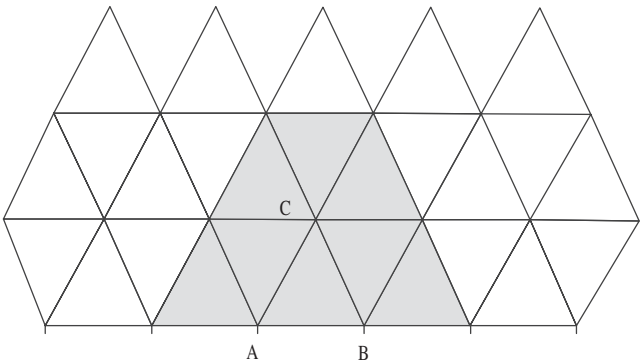

Figure 2. Space averaging region for exit angle estimation at outflow boundary edges.

boundary transparency. The set of boundary conditions is expressed by

$$\begin{bmatrix} \eta^+ \\ q_x^+ \\ q_y^+ \end{bmatrix} = \begin{bmatrix} \eta^- \\ c_g \eta^- \cos\theta \\ c_g \eta^- \sin\theta \end{bmatrix} \tag{14}$$

where θ is the outflow angle, which coincides with the initial angle of incidence in the case of propagation over an horizontal bottom and in the absence of obstacles. In the presence of obstacles and/or irregular bathymetry, the exit angle is not known and thus a space and time averaged angle is calculated for each boundary edge at run-time, based on the previous known values of the velocity components at the surrounding cells. Combinations of different averaging formulas and regions were investigated and assessed for oblique wave propagation over on open domain with uniform bed topography. The combination which performed best, and which was eventually adopted as the transparent boundary condition, consists of the averaging formula (15) applied over an averaging region as illustrated in Figure 2.

$$\bar{\theta} = \tan^{-1}\left(\frac{\sum_{i=1}^{ncv}\sum_{j=1}^{ndt} q_{y,i,j}}{\sum_{i=1}^{ncv}\sum_{j=1}^{ndt} q_{x,i,j}}\right) \tag{15}$$

where *ndt* is the number of time steps from the time of velocity component collection (which is taken to be the arrival of the disturbance at the particular outflow boundary cell) until the current time, t, and *ncv* are the cells constituting the averaging region.

For a general outflow boundary edge, AB, the velocity components are collected at every time step for the shaded cells, i.e. the cells that have at least a common vertex with the triangle ABC to which edge AB belongs. In this case $ncv = 8$. The computed average angle is adopted as the exit angle for both nodes A and B.

A well-posedness analysis is meaningless, both for the $U^+ = U^-$ boundary condition and for condition (14), since in both cases no external quantity is imposed but instead internal information is used. However, in the latter case the solution $Q = c_g\eta$ is imposed, resulting in a fairly effective transparent boundary condition (as will be shown later).

4.3. Fully reflective (impermeable wall) boundary conditions

The velocity normal to a rigid, impermeable, fully reflecting boundary in the domain must be zero. The following exterior (+) Riemann states are therefore imposed along solid boundaries:

$$\begin{bmatrix} \eta^+ \\ u^+ \\ v^+ \end{bmatrix} = \begin{bmatrix} \eta^- \\ 0 \\ v^- \end{bmatrix} \tag{16}$$

where u and v are the q_x and q_y components with respect to the edge-local co-ordinate system. The u and v are then transformed back to the global co-ordinate system. Work is currently undergoing on implementing partially reflective boundaries by incorporating an energy-dissipative region in front of the wall [18]. The width and dissipation factor within this layer affect the absorbed and reflected energy.

4.4. Treatment of lateral boundaries for normal wave incidence

Rectangular domains are often encountered in 2D coastal wave modelling. For oblique wave incidence, there exist two driving boundaries (hence use of Equation (13)) and two outflow boundaries (hence use of Equations (14) with (15)). For normal incidence there exists one driving, one outflow and two lateral boundaries. Lateral boundaries can either be treated using Equation (13) or using Equations (14) and (15).

In cases where the major part of the 'flow' is along a lateral boundary, a 'far field' situation can be assumed. Equation (13) can then be used to drive the lateral boundary, assuming that η remains unaffected by the flow conditions in the interior of the domain. In that way the characteristic requirements are only violated at the downwave outflow boundary, and use of (13) will produce more accurate results but will also partially reflect back into the domain the outgoing disturbance. This implies that the simulation must not be carried out for a very long time and the computation must be terminated before numerical reflections reach the area of interest.

When the major part of the 'flow' is across a lateral boundary then Equation (13) will create significant reflections, and it is preferable to use Equations (14) and (15).

5. TIME INTEGRATION

The values of the conserved variables at the next time level are computed from Equation (7), which may be expressed as

$$\frac{(UV)_i^{n+1} - (UV)_i^n}{\Delta t} = -[\alpha R(U_i^{n+1}) + (1-\alpha)R(U_i^n)] \tag{17}$$

where U_i^{n+1} is the vector of variables for cell i at time level $n+1$, U_i^n is the known state at time level n, Δt is the time step, V_i is the area of cell i (constant with respect to time for a non-adaptive scheme) and $R(U_i^n)$ is the right-hand side of Equation (7) evaluated as described in the previous sections. When $\alpha = 0$, Equation (17) is the Euler explicit scheme, when $\alpha = 1$, it is the first-order Euler implicit scheme, and when $\alpha = 0.5$, it is the second-order trapezoidal implicit scheme.

In explicit time integration the variables are updated in time based solely on the values at the previous time level. Results from explicit time integration were not satisfactory (see Sections 6.1 and 6.2) and in addition this approach required very small time steps. Consequently the more accurate implicit time integration was implemented. For $\alpha \neq 0$ it can be seen from Equation (17) that in order to compute the unknown state, U_i^{n+1}, the value of R at that state is required, hence the implicit feature of the scheme.

Another important characteristic of the implicit formulation is that the value of R for cell i at time $n+1$ depends not only on the values of the variables (U) for that cell but also on those for the adjacent cells.

Solution of the implicit Equation (17) is achieved by linearizing it using Newton's method [19], whereby the unknown quantities, U_i^{n+1}, are approximated by a known state, U_i^s, plus an error quantity, ΔU_i^s, for all cells i, where s is a subiteration index. Substituting Equations (4) and (5) of Anastasiou and Chan [10] into Equation (7) of the present paper, recalling that $J = \partial F/\partial U$ is the flux Jacobian, and applying Newton's linearization in Equation (17), yields the following implicit formulation for a cell in the domain:

$$\begin{aligned}
&\left[\frac{V_0}{\Delta t} I + \alpha \sum_{p=1}^{3} \frac{1}{2}(J_0 + |A_{0,p}|)\Delta l_{0,p} + V_0 \frac{\partial G_0}{\partial U_0^{n+1}}\right] \Delta U_0^s \\
&\quad + \sum_{q=1}^{3} \left[\alpha \frac{1}{2}(J_q - |A_{0,q}|)\Delta l_{0,q}\right] \Delta U_q^s \\
&\quad = -\left[\frac{V_0}{\Delta t}(U_0^s - U_0^n) + \alpha R(U_0^s) + (1-\alpha) R(U_0^n)\right]
\end{aligned} \tag{18}$$

where 0 denotes the particular cell and 1, 2, 3 denote its adjacent cells, subscripts i, j refer to the interface between cells i and j, and I is the identity matrix. The source Jacobian can be found to be from Equation (6)

$$\frac{\partial G_0}{\partial U_0^{n+1}} = \begin{bmatrix} 0 & \partial(c/c_g)/\partial x & \partial(c/c_g)/\partial y \\ \partial(cc_g)/\partial x & 0 & 0 \\ \partial(cc_g)/\partial y & 0 & 0 \end{bmatrix} \tag{19}$$

Equation (18) demonstrates clearly the cell-coupling effect of the implicit scheme. The implementation of the phantom cells allows treatment of boundary cells in exactly the same manner as that appropriate for the interior cells. Application of Equation (18) to all cells in the domain results in a matrix equation of the type $Bx = C$ where B is a $N \times N$ matrix, with only 4 non-zero (not necessarily consecutive) entries per row, and x, C are $N \times 1$ matrices ($N =$ number of cells in domain). Each of the elements in B, x and C is a 3×3 matrix. Direct inversion of B would require excessive computational resources. Instead, the fully discretized implicit time integration equation is written as

$$(D_{\text{diag}} + L_{\text{low}} + U_{\text{up}})\Delta U^s = \text{RHS} \tag{20}$$

where D_{diag} is a block diagonal matrix, L_{low} is a block lower triangular matrix, and U_{up} is a block upper triagonal matrix, with each of the elements in these matrices being a 3×3

matrix. The approximate LU factorization (ALU) scheme as proposed by Pan and Lomax [20] is then adopted to convert the implicit Equation (20) into the form

$$(D_{\text{diag}} + L_{\text{low}})D_{\text{diag}}^{-1}(D_{\text{diag}} + U_{\text{up}})\Delta U^s = \text{RHS} \tag{21}$$

where the error of factorization is equal to $L_{\text{low}}D_{\text{diag}}^{-1}U_{\text{up}}\Delta U^s$. ΔU^s may now be obtained in a straight forward manner with minimum computing storage and time requirements since the inversion of $3N$, 3×3 matrices is required rather than the inversion of one, $3N \times 3N$ super-matrix. Subiterations within each time step are commenced by setting $U_i^s = U_i^n$ and are terminated when the $L2$ norm of the iteration process,

$$L2 = \left[\frac{1}{N}\left(\sum_{i=1}^{N}(\Delta U_i^s)^2\right)\right]^{1/2} \tag{22}$$

is less than a specified tolerance value (usually 10^{-4}). As ΔU^s tends to zero, U_i^s tends to the time accurate U_i^{n+1}, and at the same time the ALU factorization error tends to zero. In most cases 2–3 subiterations are required per time step.

The following relation has been adopted for the computation of the time step for the implicit scheme:

$$\Delta t = \frac{1}{N}\sum_{i=1}^{N}\left\{\min_{j=k(i)}\left(C_{fl}\,\frac{0.5\,s_{i,j}}{c_i}\right)\right\} \tag{23}$$

where N is the total number of cells in the domain, $k(i)$ is a list of the three adjacent cells to cell i, C_{fl} is a user specified Courant-like number (sensible range: $0.25 \leqslant C_{fl} \leqslant 1.75$), $s_{i,j}$ is the distance between the centres of the adjacent cells i and j, and c_i is the wave celerity at cell i. The time step value for the implicit scheme is generally one order of magnitude larger than the feasible time step in the explicit time integration formulation.

Finally, it must be noted that for the cases tried better results were obtained using the second-order trapezoidal time integration ($\alpha = 0.5$) compared with the fully implicit time integration ($\alpha = 1.0$) and hence the former has been adopted in order to obtain the results described in the present study.

6. NUMERICAL RESULTS

The linear model was tested for a variety of nearshore wave propagation problems. In all cases the stillwater depth, d, at each cell centre was computed from the bathymetry input grid according to the following inverse-power interpolation technique:

$$d_i = \sum_{j=1}^{n}\frac{d_j}{S_{i,j}^m}\Bigg/\sum_{j=1}^{n}\frac{1}{S_{i,j}^m} \tag{24}$$

where, $S_{i,j}$ is the distance between the centre of cell i and the bathymetry input point j, m is an integer specifying the power of interpolation and n is the number of points used in the interpolation. High values of m result in sharper bottom variation. In the present algorithm, m is set to 2 and n to 3.

Table I. Maximum, average and standard deviation of the error in an open domain, uniform depth ($d = 1$ m), sinusoidal wave with $H_{in} = 0.06$ m, $T = 0.8$ s, simulation for 100 s.

Incident angle (deg)	Mesh density (nodes/L)	Errors in wave height as predicted from finite volume formulations (in %)	
		Explicit time integration	Implicit time integration
0	10	Max: 17.73, avg: 4.99, std: 3.58	Max: 6.23, avg: 1.65, std: 1.28
0	20	Max: 5.33, avg: 1.53, std: 1.22	Max: 1.51, avg: 0.35, std: 0.25
30	10	Max: 13.70, avg: 3.58, std: 2.54	Max: 10.51, avg: 4.69, std: 1.92
30	20	Max: 7.16, avg: 1.36, std: 1.18	Max: 2.22, avg: 0.78, std: 0.42
45	10	Max: 8.63, avg: 2.67, std: 1.79	Max: 13.75, avg: 5.92, std: 2.24
45	20	Max: 5.29, avg: 1.02, std: 0.87	Max: 2.94, avg: 1.00, std: 0.46
60	10	Max: 13.09, avg: 3.01, std: 2.26	Max: 14.71, avg: 5.82, std: 2.62
60	20	Max: 6.71, avg: 1.15, std: 1.03	Max: 3.15, avg: 0.99, std: 0.52
75	10	Max: 15.83, avg: 3.34, std: 2.51	Max: 14.59, avg: 6.04, std: 2.66
75	20	Max: 5.85, avg: 1.13, std: 0.96	Max: 3.05, avg: 1.07, std: 0.52
Average errors	10	Max: 13.80, avg: 3.52, std: 2.54	Max: 11.96, avg: 4.82, std: 2.14
	20	Max: 6.07, avg: 1.24, std: 1.05	Max: 2.57, avg: 0.84, std: 0.43

Furthermore, the wave height, H, for each cell was calculated from the surface elevation time series according to

$$H_i = 2(2\overline{\eta_i^2})^{1/2} \tag{25}$$

where the overbar denotes time averaging. Collection of η was started after one full period had elapsed from the time instant when the wave first reached the point furthest away in the domain, and continued until the pre-specified termination time was reached. The option of calculating H_i with the zero up-crossing method has also been included. According to this method a user defined number of initial waves may be neglected and H_i computed as the average of another user defined number of successive up-crossings of zero. Once the specified number of waves has been collected for each cell the program automatically terminates. This 'auto-termination' switch may be used as a safeguard against unwanted contamination of results in the area of interest by potential reflections. All simulations were carried out on a desktop PC with 128 MB SDRAM and an Intel PII CPU running at 333 MHz. The execution time of each simulation is denoted as t_{CPU}.

6.1. *Wave propagation over an horizontal bed*

The simplest possible propagation problem was initially examined. Regular waves were propagated for 100 s over an open 4 m × 3 m domain with 1 m uniform depth. The incident wave had height $H_{in} = 0.06$ m, and period $T = 0.8$ s. Mesh densities corresponding to 10 (coarse mesh) and 20 (fine mesh) nodes per wavelength were tried. In the implicit formulation, time steps equal to 0.02 and 0.01 s for the coarse and fine meshes, respectively, were used, whereas in the explicit formulation, time steps equal to 0.004 s for the coarse and 0.001 s for the fine mesh were used. Results were obtained for five different angles of incidence and the maximum, average and standard deviation of error in the domain were computed (see Table I).

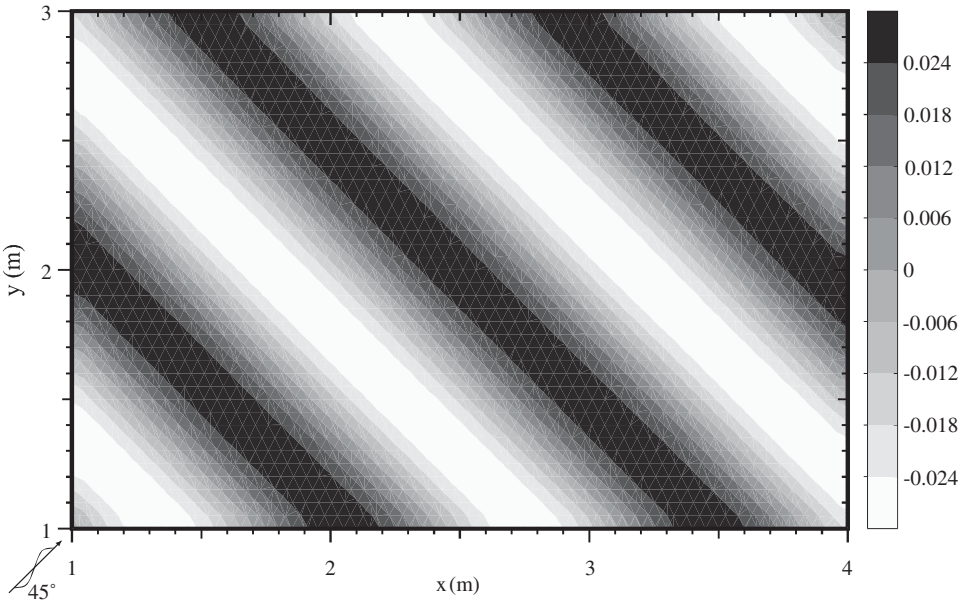

Figure 3. Surface elevation contour plot for 45° incidence, $H_{in} = 0.06$ m, $T = 0.8$ s, 1 m uniform depth, 20 nodes per wavelength, at $t = 100$ s.

The error for a cell, i, is calculated from

$$(\text{Error}\%)_i = \frac{|H_i^{\text{predicted}} - H_i^{\text{analytical}}|}{H_i^{\text{analytical}}} 100 \tag{26}$$

From the last row of Table I it is evident that for the fine mesh the errors are significantly lower for the implicit formulation. The fact that the explicit formulation gives a lower average error for the coarse mesh is an indication that the implicit formulation requires a higher than 10 nodes per wavelength resolution (approximately 15 nodes per wavelength). Furthermore, both formulations are seen to be consistent with the governing equations in the sense that the errors associated with the fine mesh are lower than those associated with the coarse mesh for all incident wave angles.

The surface elevation contour plot for wave propagation at 45°, based on the implicit formulation and 20 nodes per wavelength, is presented in Figure 3. The contours are straight and parallel as expected. For this run, the percentage error in the average wave height in the domain (a measure of the energy present in the domain) was output at each time step for a long simulation time (1600 s = 2000 wave periods) and is shown in Figure 4. It may be seen that the insignificant error oscillations (e.g. amplitude of error oscillation $B \approx 0.06\%$) keep amplifying with time (see profiles A, B and C) but assuming that this pattern persists, an unrealistically long simulation time is required before a significant increase in instantaneous error is obtained. More importantly, η is collected throughout the computation time for the calculation of H, and hence the error oscillations cancel out resulting in an average error of about 1% (as Table I also suggests). Figure 4 shows that the outflow boundary conditions do not reflect back into the domain any of the outgoing wave energy.

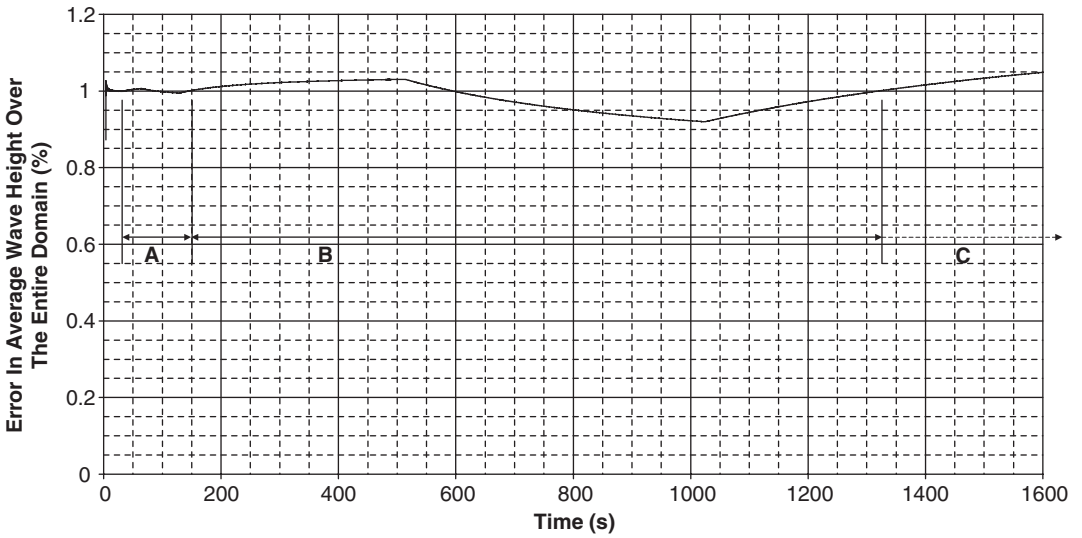

Figure 4. Measure of average energy present in the domain for 45° incidence, $H_{in} = 0.06$ m, $T = 0.8$ s, 1 m uniform depth, 20 nodes per wavelength, up to $t = 1600$ s ($= 2000$ T).

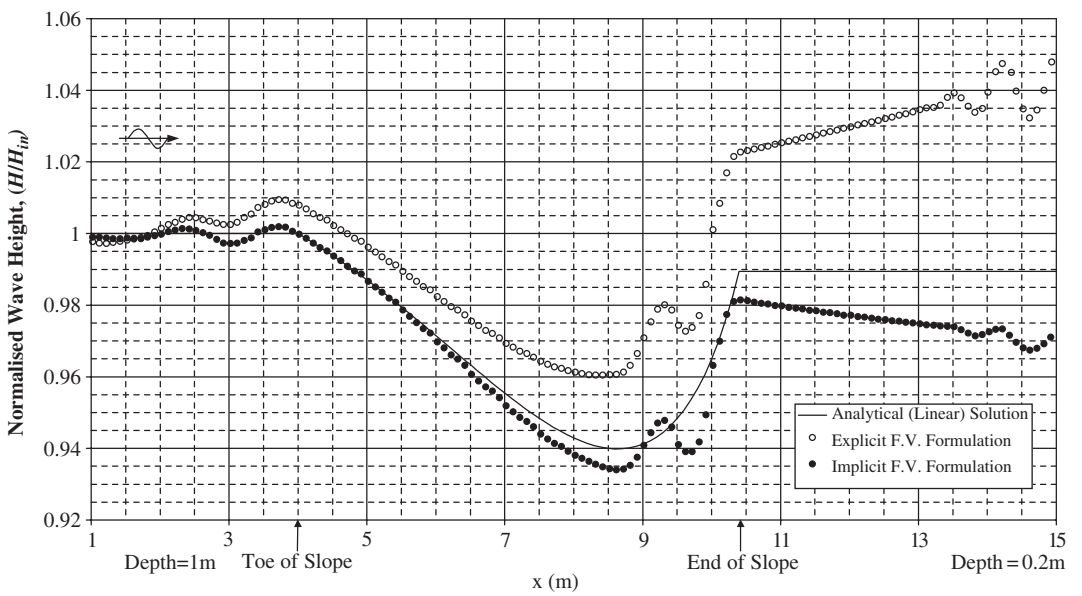

Figure 5. Wave height transformation over a 1:8 sloping linear talud, normal incidence, $H_{in} = 0.06$ m and $T = 1.3$ s.

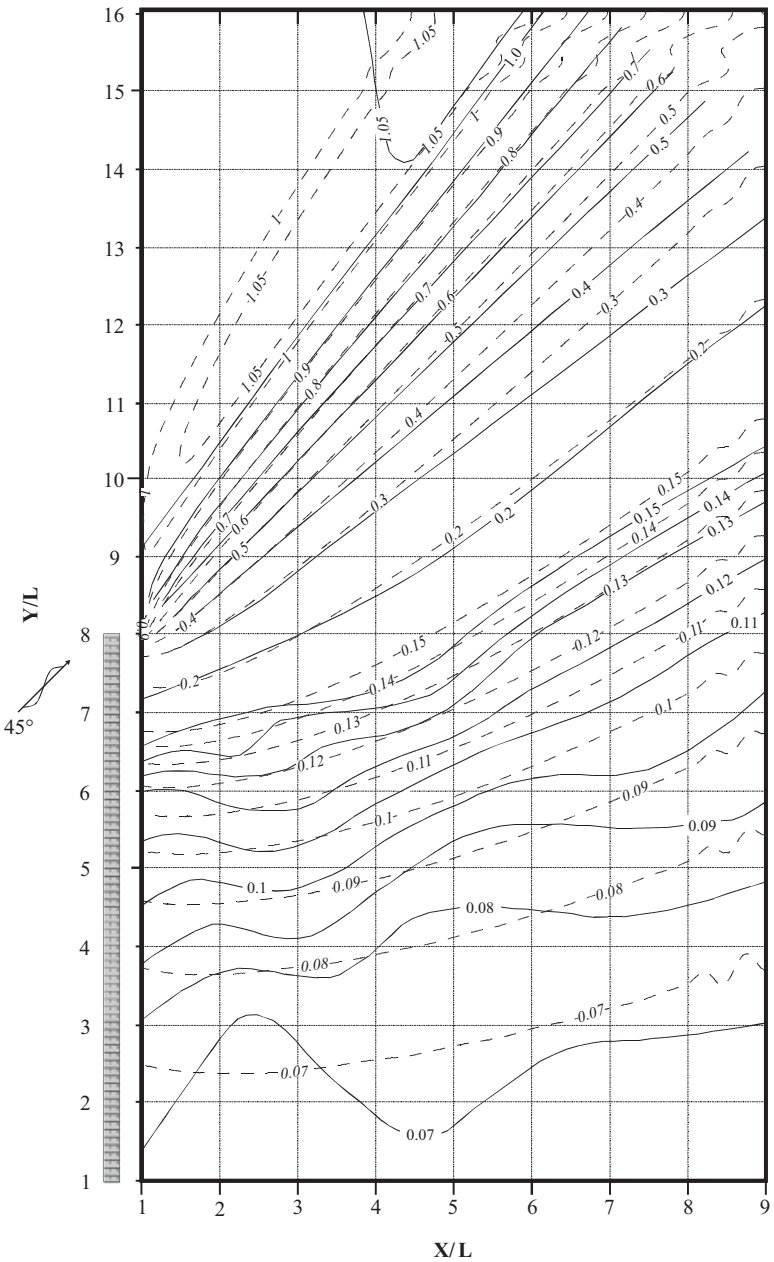

Figure 6. Normalized wave height contours for 45° incidence relative to a semi-infinite breakwater (solid: analytical [21]; dashed: linear predictions).

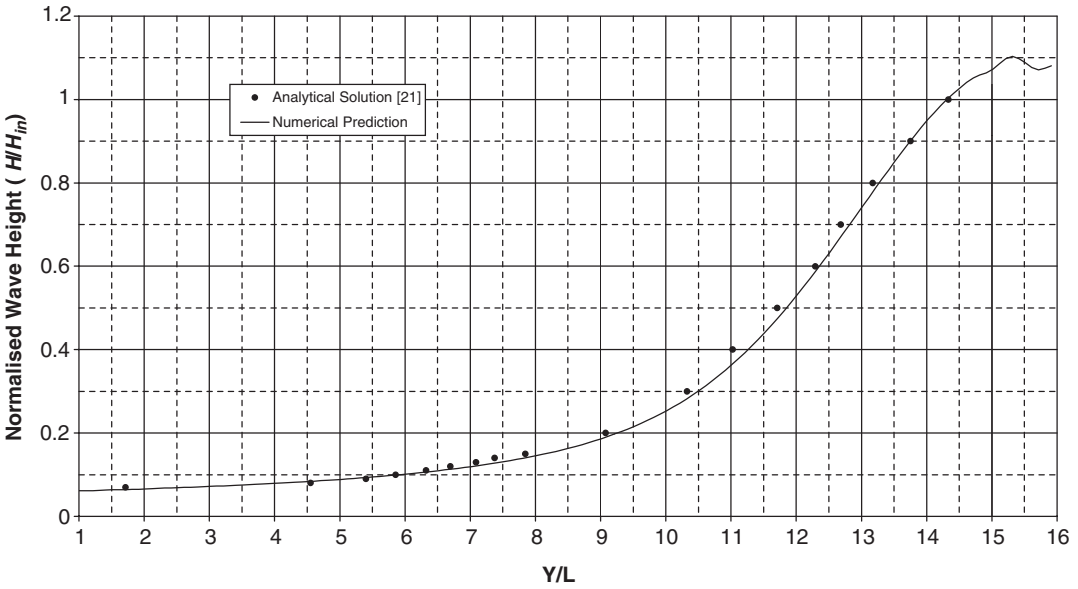

Figure 7. Normalized wave height at a distance $4L$ behind the semi-infinite breakwater (i.e. at $x = 5L$), 45° incidence.

The above results corresponded to deep water conditions. In intermediate and shallow waters the errors were similar to those in deep water, with the errors gradually increasing as the water depth reduced. However, the average spatial error remained below the 2.5% margin for 20 nodes per wavelength and for all angles of incidence tested. Furthermore, it must be noted that slightly better agreement was achieved for a more linear wave train with $ak = 0.094$ (for $H_{\text{in}} = 0.03$, $T = 0.8$ s) rather than the one used to obtain the above results which had $ak = 0.188$.

6.2. *Wave shoaling over a linear talud*

Regular waves were also propagated over an open 14 m × 10 m domain with a linear talud bathymetry (plane slope, each end of which is connected to a constant depth region) consisting of a 1:8 slope starting at $x = 4$ m, with a depth equal to 1 m, and ending at a depth equal to 0.2 m. The analytical (linear, pure shoaling) solution for the particular bathymetry and incident wave exhibits a turning point (see Figure 5) providing thus an interesting test case. The incident wave train had $H_{\text{in}} = 0.06$ m, $T = 1.3$ s and normal incidence to the slope. The domain consisted of 28 000 cells (14 241 nodes) giving on average 22 nodes per wavelength. The conditions given in Equation (13) were used at the driving and lateral boundaries. At the downwave boundary the conditions given in Equations (14) and (15) were deployed. In Figure 5 the normalized wave height along the centreline of the domain (in the direction of wave incidence) is shown.

Time steps of 0.001 and 0.012 s were used in the explicit and implicit finite volume formulations, respectively. The oscillations in both formulations over the slope (i.e. for $9 \leqslant x \leqslant 10$)

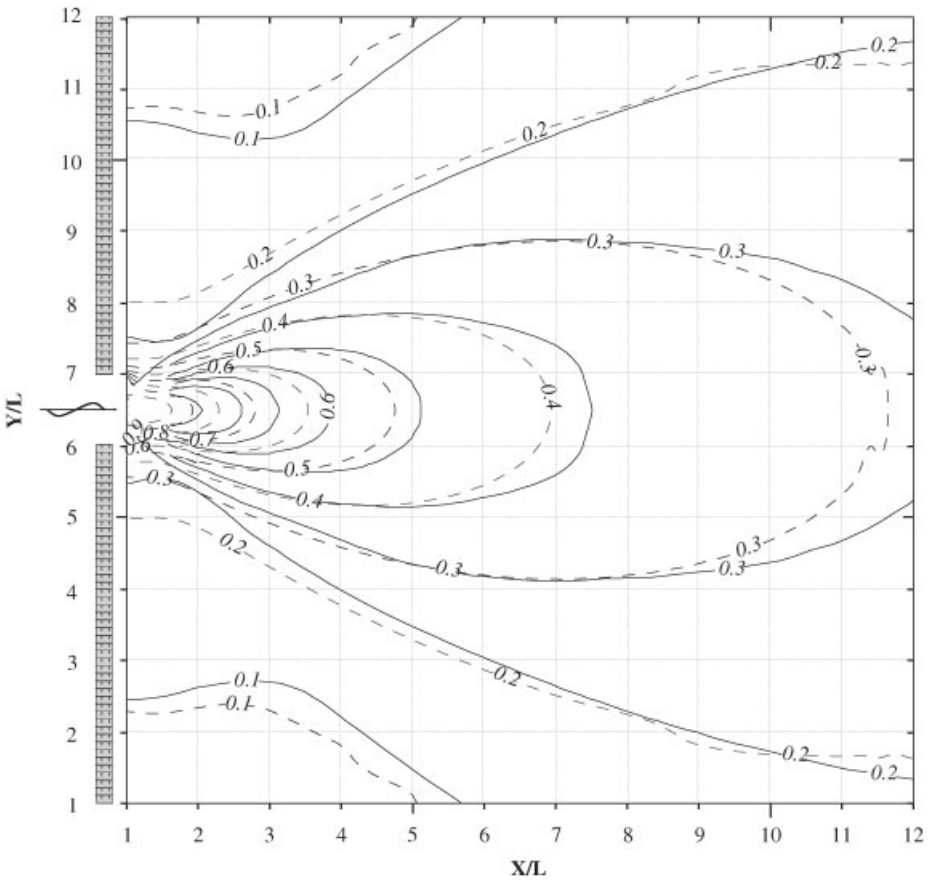

Figure 8. Normalised wave height contours for normal wave incidence onto a breakwater gap of width equal to 1L (solid: analytical [22]; dashed: linear predictions).

may be attributed to slope reflections. The results were compared with the 2D linear analytical solution and the errors (from Equation (26)) were found to be:

- Explicit finite volume formulation: max: 5.93%, avg: 1.57%, std: 1.34%.
- Implicit finite volume formulation: max: 2.84%, avg: 0.45%, std: 0.47%.

For the explicit formulation $t_{\mathrm{CPU}} = 58.9$ min, while for the implicit scheme $t_{\mathrm{CPU}} = 21.4$ min owing to the fact that larger time steps can be used in the implicit scheme. The errors associated with the implicit formulation are significantly lower than those of the explicit formulation. Furthermore, the failure of the explicit formulation to model shoaling is evident from Figure 5, and thus it was decided to stop using the explicit formulation. All the numerical results presented in the following sections have been obtained based on the second-order trapezoidal implicit formulation.

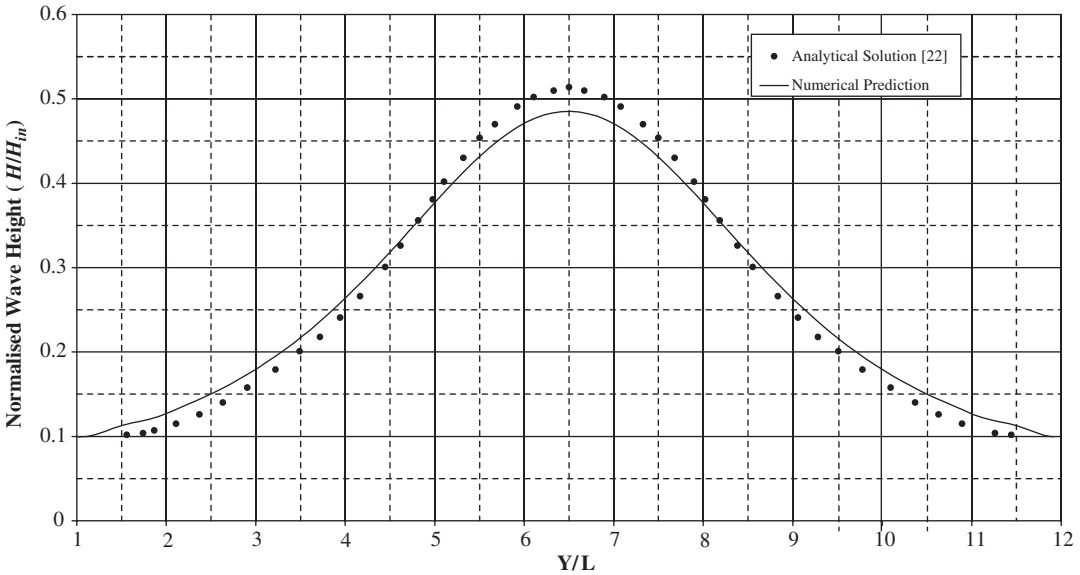

Figure 9. Normalized wave height at a distance $4L$ behind the two semi-infinite breakwaters (i.e. at $x = 5L$), normal incidence.

6.3. *Wave diffraction behind a semi-infinite breakwater and through a breakwater gap*

The diffraction of a regular wave train propagating in the lee of a semi-infinite breakwater and also through a breakwater gap has been studied numerically for different angles of incidence. Due to space limitations, the results from two configurations are only presented. In both cases, the mesh density was 20 nodes per wavelength, $\Delta t = 0.01$ s, $H_{\text{in}} = 0.03$ m, $T = 0.8$ s, $d = 1$ m throughout.

The computed ($t_{\text{CPU}} = 163.8$ min) normalized wave height contours for a semi-infinite breakwater at 45° wave incidence, can be seen in Figure 6, plotted against the analytical contours. Some oscillations in the proximity of the outflow boundaries can be observed, which stem from the increased numerical error for low outflow velocities. This error is in turn introduced into the exit angle estimation through Equation (15). Thus, the oscillations become more conspicuous towards the more sheltered regions, where the wave heights and hence wave velocities are low. In order to obtain a better insight, the predicted and analytical normalized wave heights along a section parallel to the breakwater and at a distance $4L$ (i.e. at $x = 5L$) are shown in Figure 7. Agreement between linear predictions and analytical solutions is seen to be very good.

The computed ($t_{\text{CPU}} = 133.6$ min) normalized wave height contours for a breakwater gap configuration at normal wave incidence are shown in Figure 8. For gap widths in excess of about $5L$, the diffraction patterns at either side of the opening are more or less independent of each other [22]. A relatively narrow gap, equal to $1L$, was therefore selected with a view to providing a good indication of the interacting diffraction patterns in the lee of the two semi-infinite breakwaters. Agreement between predictions and analytical solutions is seen to be fairly good, with the predictions underestimating the energy spreading along the centreline

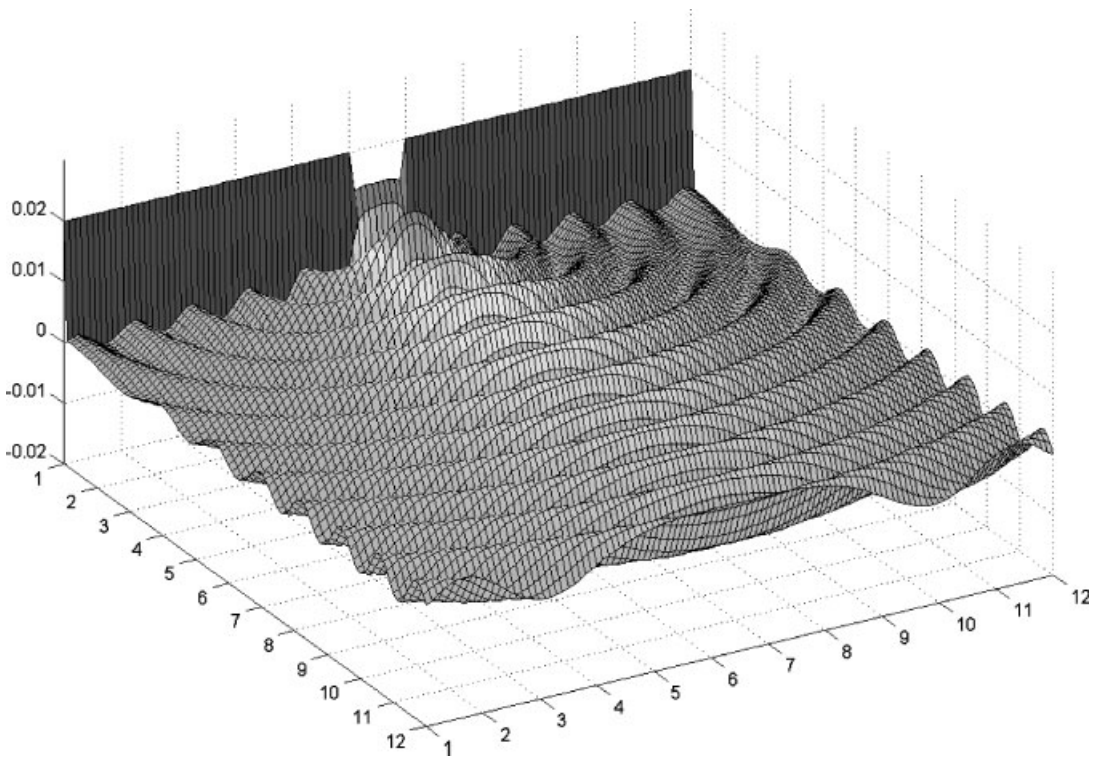

Figure 10. 3D surface elevation snapshot behind a breakwater gap of width equal to $1L$, normal incidence, $H_{in} = 0.03$ m, $T = 0.8$ s, at 11.4 s.

and generally overestimating it in the transverse direction away from the centreline. This is also evident in Figure 9, where the results for the section at $x = 5L$ are also shown. Underprediction at the peak for that section is 5.58%. The 3D surface elevation at time 11.4 s is shown in Figure 10.

6.4. Combined refraction–diffraction in the vicinity of an elliptic shoal

In order to further verify the model, numerical predictions were compared with the experimental data of Berkhoff *et al.* [23]. The bathymetry consisted of an elliptic shoal resting on a 1:50 plane sloping seabed. The entire slope is turned at an angle of 20° with respect to the wave paddles. The bathymetry and computational domain used are shown in Figure 11. The average mesh density was 15 nodes per wavelength, the time step interval $\Delta t = 0.012$ s, the incident wave height $H_{in} = 0.0464$ m, and the wave period $T = 1.0$ s. The conditions given in Equation (13) were used at the driving and lateral boundaries, and the conditions given in Equations (14) and (15) were deployed at the downwave boundary. The execution time, t_{CPU}, for this run was equal to 208.7 min.

For brevity, the normalized wave heights along Sections 3, 4, 6 and 7 only are given, see Figs. 12(a)–12(d). In Section 3, the peak is overestimated by 8% and significant depressions

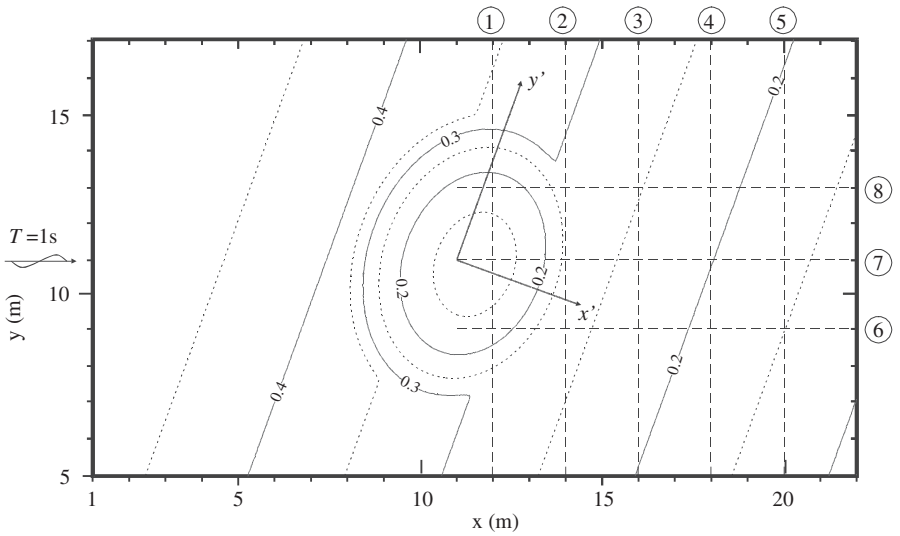

Figure 11. Topography and computational domain for the experiment of Berkhoff *et al.* [23]. Dashed lines and labels indicate the various sections (centre of shoal at $\{11, 11\}$ metres).

on each side of the peak are predicted which are not physically present. In Section 4, the computed peak is in good agreement with the measured one but the profile around the peak is predicted narrower than that measured. Furthermore, the side lobes are predicted higher than observed. In the longitudinal Section 6, the numerical model fails to predict the wave height depression around $x = 19.5$ m. In Section 7, it may be seen that focusing is predicted to occur sooner and that the shoreward wave height distribution is underestimated.

The presented results suggest that the model is capable of simulating satisfactorily wave transformation over bathymetries instigating wave focusing.

6.5. Investigation of paraxiality in the vicinity of a submerged circular shoal

In this section, results for the numerical experiment of Kirby [5] are presented and discussed. Waves were propagated over a circular shoal placed on an horizontal seabed at 0° and 45° angles of wave incidence ($H_{\text{in}} = 0.0464$ m, $T = 1$ s). In both cases the mesh density was on average 13 nodes per wavelength. A finer mesh was not used since in this case the ability of the model to reproduce results for different angles of incidence over the same bathymetry was investigated rather than the actual accuracy of the results.

The surface elevation for 0° and 45° wave incidence can be seen in Figures 13 and 14, respectively. The execution time, t_{CPU}, was 119.6 min for the 0° wave incidence and 203.9 min for the 45° wave incidence. The execution time was longer in the latter case since the wave train had to travel a longer distance (the diagonal of the domain) until it triggered the 'auto-termination' switch. It is evident that in both cases wave focusing occurs behind the shoal centre in the direction of wave propagation, and very symmetrically with respect to it. The resulting normalized wave height contours are superimposed in Figure 15. The 45° results were rotated by exactly 45° clockwise and translated $+5$ m in the y-axis so that the two

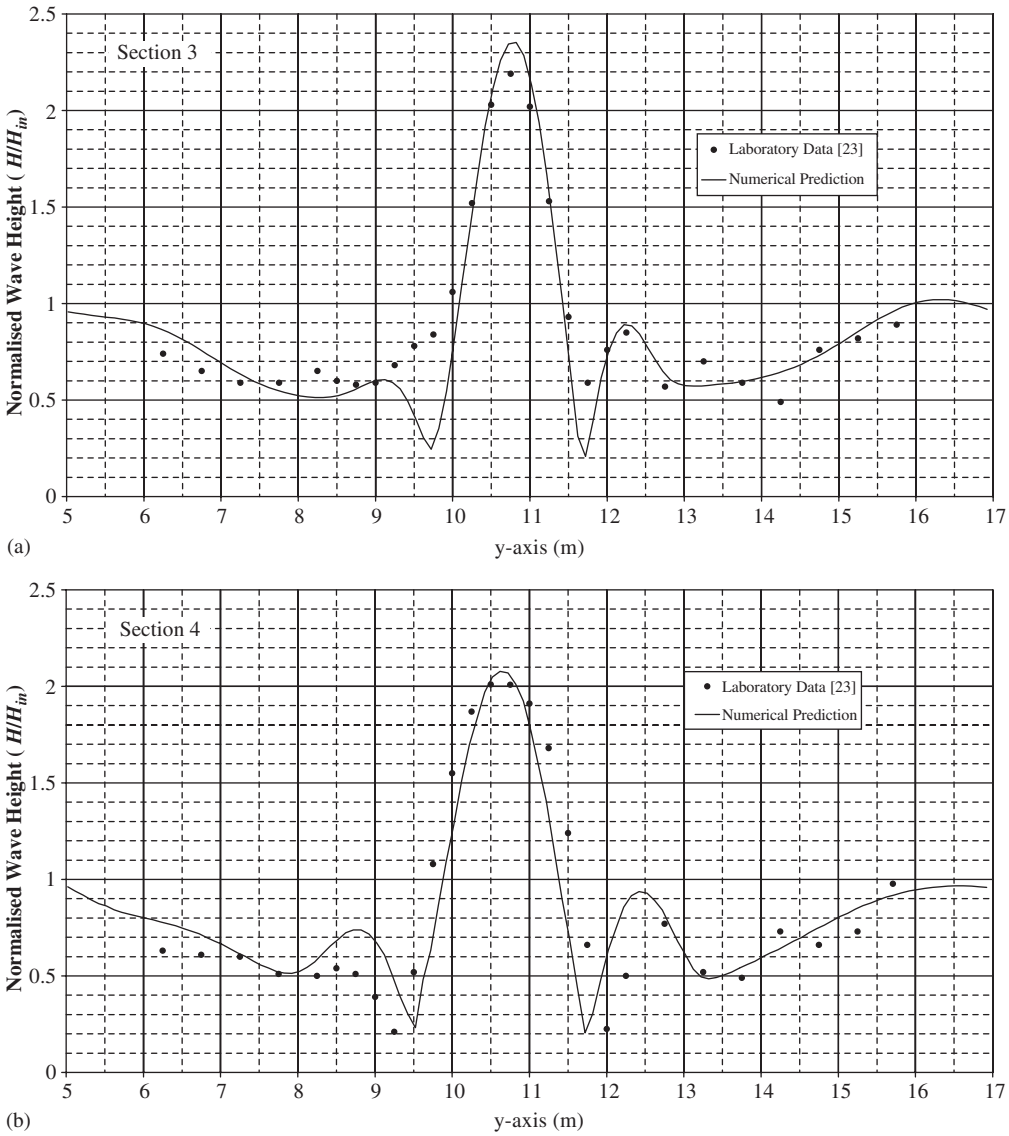

Figure 12. Comparison of numerical predictions with the experimental data of Berkhoff *et al.* [23]: (a) transverse section 3 along $x = 16$ m; (b) transverse Section 4 along $x = 18$ m; (c) longitudinal Section 6 along $y = 9$ m; and (d) longitudinal Section 7 along $y = 11$ m.

shoals coincided. We see that the wave height contours are in very good agreement for the two cases, any slight differences attributed to the different orientation of the wave fronts in each case with respect to the computational cell edges. The evidence presented suggests that the model is paraxiality-free. On the contrary, Kirby's [5] parabolic model (enhanced for

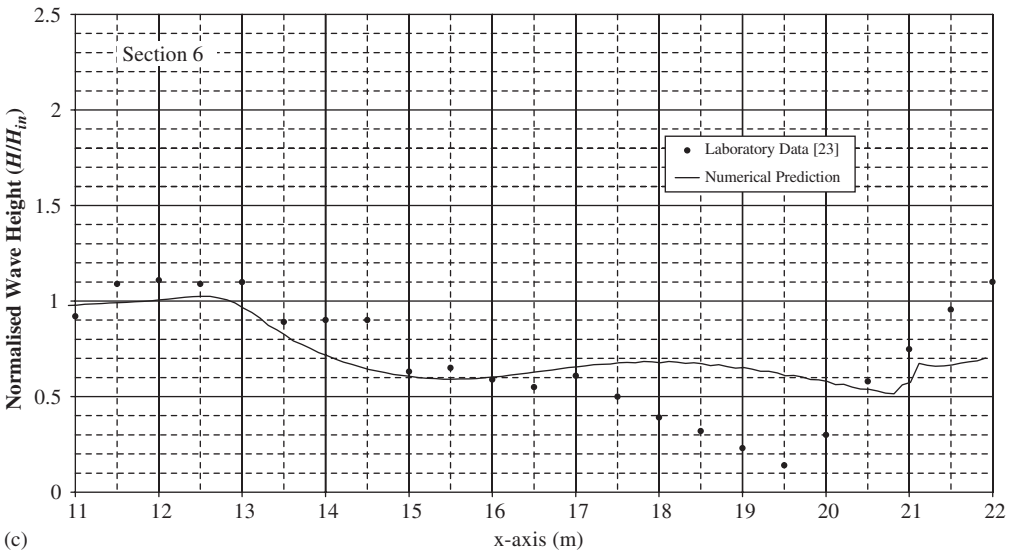

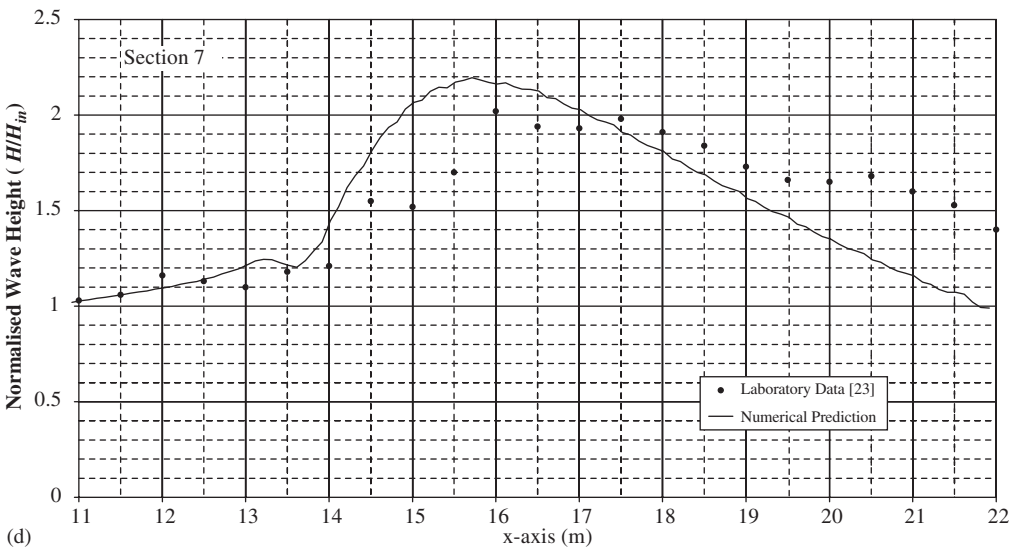

Figure 12. *Continued.*

large angle wave propagation), exhibits a distinctive surface elevation asymmetry at 45°, for the 70° minimax approximation, which is absent at normal incidence. Furthermore, Kirby [5] rotated the normalized wave height contours by 39.75° instead of 45°, so as to forcefully align the focusing points of the two cases, and even by doing so he did not obtain results as good as the ones presented in Figure 15.

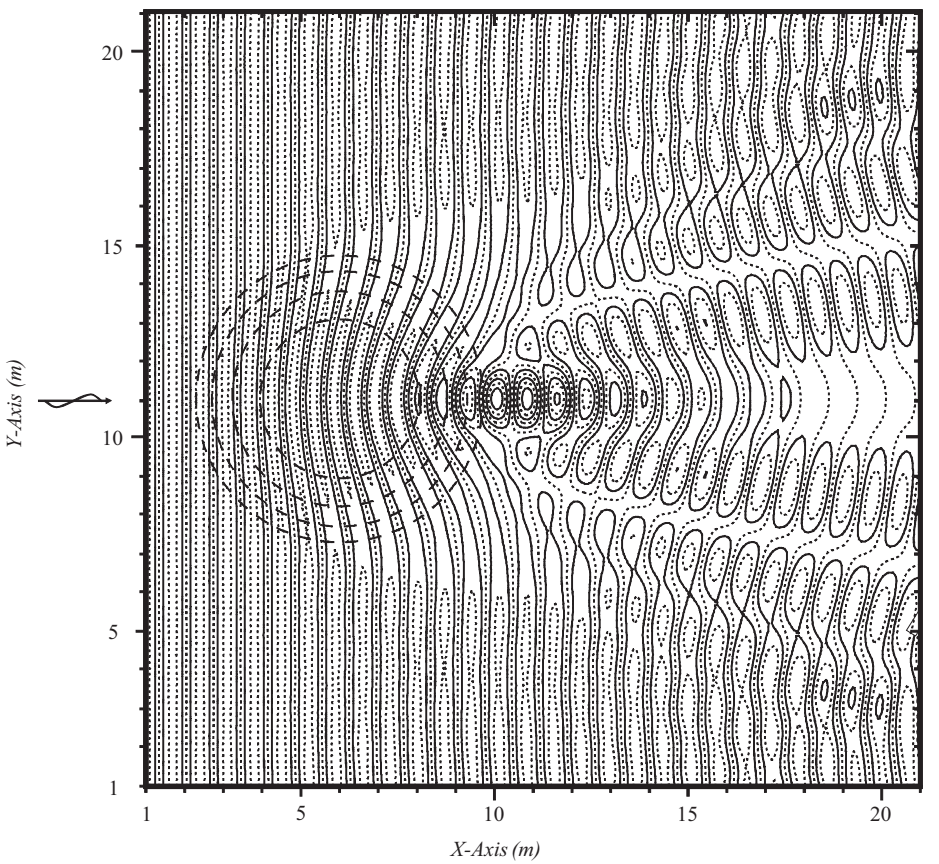

Figure 13. Surface elevation plot over the circular shoal for normal wave incidence (centre of shoal at $\{6, 11\}$ metres).

7. CONCLUSIONS

The development of a versatile finite volume solver for the harmonic hyperbolic form of the 2D depth-integrated mild-slope equation has been presented. Unstructured triangular meshes have been employed, able to discretize effectively irregular domains. A distinctive feature of the present methodology is the construction of Roe's flux function through each side of a triangular cell by considering a 1D local Riemann problem. The eigensystem required for the construction of Roe's matrix has been derived. Second-order accuracy in space has been obtained by considering a linear variation of the conserved variables within each internal triangular cell.

Boundary conditions for driving boundaries have been derived by applying a zero-order space extrapolation of the characteristic variables. Transparent boundary conditions have been formulated by computing the wave exit angle at run time and imposing the solution $Q = c_g\eta$ of the mild-slope equation. Setting the external Riemann state u^+ equal to zero has achieved effective simulation of fully reflective boundaries.

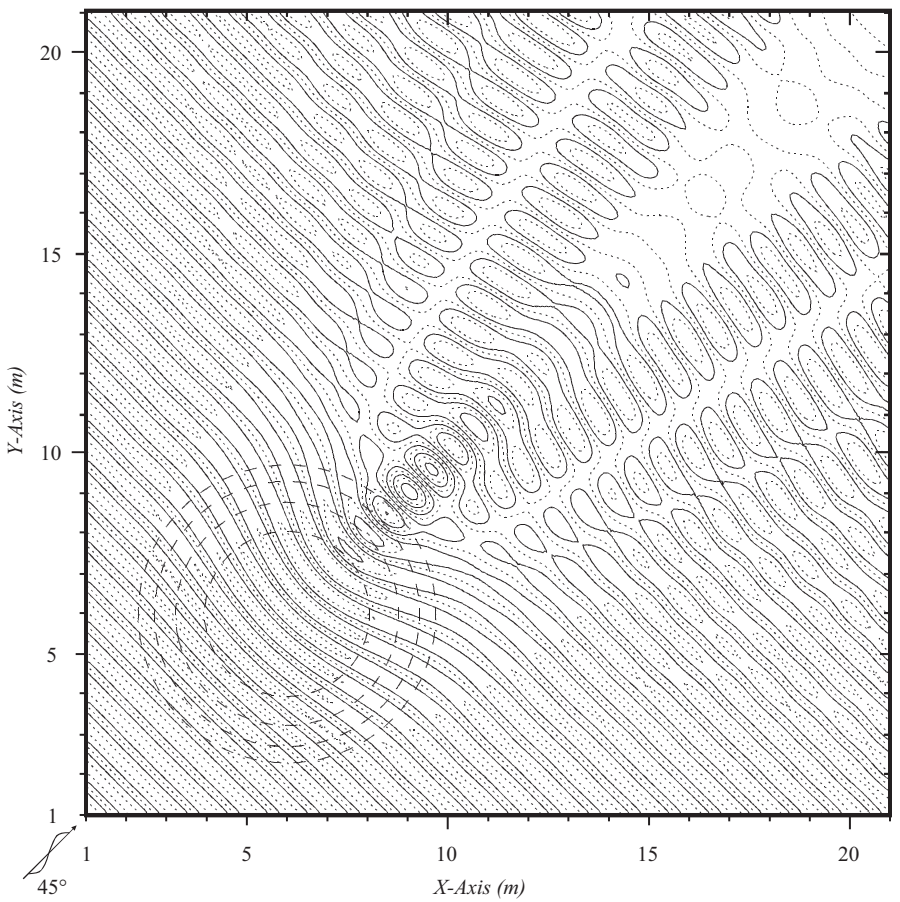

Figure 14. Surface elevation plot over the circular shoal for 45° wave incidence (centre of shoal at $\{6, 6\}$ metres).

The formulation of a second-order accurate implicit time integration scheme has been presented in detail and its superiority as opposed to the explicit formulation has been established. Furthermore, implementation of the implicit formulation has expedited the solution process (even though 2–3 iterations per time step are executed in the implicit formulation), since the feasible time step associated with the implicit formulation is generally one order of magnitude larger than that of the explicit formulation.

The model was found to be consistent, paraxiality-free and in close agreement with available analytical results. The model can be used to predict wave transformation behind breakwaters and harbour agitation as long as the boundaries are, at this stage, fully reflecting. Comparison with experimental results has verified that the present model deals satisfactorily with bathymetries instigating wave focusing.

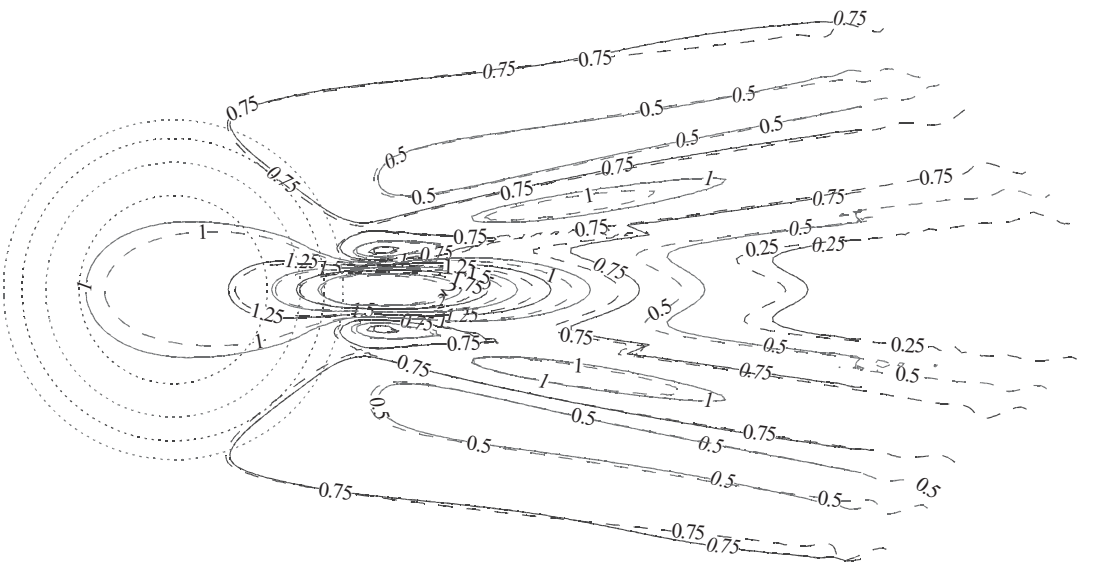

Figure 15. Normalized wave height contours and bathymetry for the circular shoal (solid: normal normal incidence, dashed: rotated 45° incidence, dotted: depth contours).

ACKNOWLEDGEMENTS

This work has been financed by the Commission of the European Communities, Directorate General for Science, Research and Development under MAST contract No. MAS3-CT97-5052 (Marie Curie Fellowship). The myriads of fruitful discussions with Dr C.T. Chan are also appreciated.

REFERENCES

1. Berkhoff JCW. Computation of combined refraction-diffraction. *Proceedings of the 13th International Conference on Coastal Engineering* 1972; 471–490.
2. Watanabe A, Maruyama K. Numerical modelling of nearshore wave field under combined refraction, diffraction and breaking. *Coastal Engineering in Japan* 1986; **29**:19–39.
3. Booij N. A note on the accuracy of the mild-slope equation. *Coastal Engineering* 1983; **7**:191–203.
4. Radder AC. On the parabolic equation method for water-wave propagation. *Journal of Fluid Mechanics* 1979; **95**:159–176.
5. Kirby JT. Rational approximations in the parabolic equation method for water waves. *Coastal Engineering* 1986; **10**:355–378.
6. Isobe M. A parabolic equation model for the transformation of irregular waves due to refraction, diffraction and breaking. *Coastal Engineering in Japan* 1987; **30**:33–47.
7. Li B, Anastasiou K. Efficient elliptic solvers for the mild-slope equation using the multigrid technique. *Coastal Engineering* 1992; **16**:245–266.
8. Copeland GJM. A practical alternative to the mild-slope wave equation. *Coastal Engineering* 1985; **9**:125–149.
9. Ito Y, Tanimoto K. A method of numerical analysis of wave propagation: application to wave diffraction and refraction. *Proceedings of the 13th International Conference on Coastal Engineering* 1972; 503–522.
10. Anastasiou K, Chan CT. Solution of the 2D shallow water equations using the finite volume method on unstructured triangular meshes. *International Journal of Numerical Methods in Fluids* 1997; **24**:1225–1245.
11. Chan CT. Computation of flows by the finite volume method as applied to unstructured meshes. *Ph. D. Thesis*, Imperial College of Science Technology and Medicine, U.K., 1997; 182.
12. Anastasiou K, Chan CT. Automatic triangular mesh generation scheme for curved surfaces. *Communications in Numerical Methods in Engineering* 1996; **12**:197–208.
13. Roe PL. Approximate Riemann solvers, parameter vectors, and difference schemes. *Journal of Computational Physics* 1981; **43**:357–372.

14. Toro EF. *Riemann Solvers and Numerical Methods for Fluid Dynamics*: *a Practical Introduction*. Springer: Berlin, 1997; 592.
15. Van Leer B. Towards the ultimate conservative difference scheme V. A second order sequel to Godunov's method. *Journal of Computational Physics* 1979; **32**:101–136.
16. Pan D, Cheng JC. A second-order upwind finite-volume method for the Euler solution on unstructured triangular meshes. *International Journal for Numerical Methods in Fluids* 1993; **16**:1079–1098.
17. Hirsch C. *Numerical Computation of Internal and External Flows*, *Computational Methods for Inviscid and Viscous Flows*, vol. 2. Wiley: New York, 1990; 691.
18. Sato N, Isobe M, Izumiya T. A numerical model for calculating wave height distribution in a harbour of arbitrary shape. *Coastal Engineering in Japan* 1990; **33**:119–131.
19. Smith GD. *Numerical Solution of Partial Differential Equations*: *Finite Difference Methods* (3rd edn). Oxford University Press: Oxford, 1985; 337.
20. Pan D, Lomax H. A new approximate LU factorisation scheme for the Reynolds-averaged Navier–Stokes equations. *AIAA Journal* 1988; **26**:163–171.
21. CERC. *Shore Protection Manual* (4th edn). U.S. Army Corps of Engineers Coastal Engineering Research Centre: Washington, DC, 1984.
22. Johnson JW. Generalised wave diffraction. *Proceedings of the 2nd International Conference on Coastal Engineering* 1952; 6–23.
23. Berkhoff JCW, Booy N, Radder AC. Verification of numerical wave propagation models for simple harmonic linear water waves. *Coastal Engineering* 1982; **6**:255–279.

